INSTITUTE OF PHYSICS PUBLISHING JOURNAL OF PHYSICS: CONDENSED MATTER

J. Phys.: Condens. Matter **18** (2006) L193–L203 doi:10.1088/0953-8984/18/15/L05

LETTER TO THE EDITOR

Surface-sensitive particle selection by driving particles in a nematic solvent

Takeaki Araki and Hajime Tanaka

Institute of Industrial Science, University of Tokyo, Meguro-ku, Tokyo 153-8505, Japan

E-mail: takeaki@iis.u-tokyo.ac.jp and tanaka@iis.u-tokyo.ac.jp

Received 7 March 2006
Published 30 March 2006
Online at stacks.iop.org/JPhysCM/18/L193

Abstract

Electrophoresis and sedimentation (or ultracentrifugation) are powerful means for separating particles, proteins, and DNA, exploiting the difference in particle charge, mass, and size. Surface properties of colloids and proteins are closely related to their physical, chemical, and biological functions. Thus, the selection of particles in terms of their surface properties is highly desirable. The possibility of replacing a simple liquid like water by a complex liquid may provide a novel route to particle separation. Here we report a new principle of surface-sensitive particle selection by using nematic liquid crystal as a solvent. When we immerse a particle in nematic liquid crystal, topological defects are formed around a particle if there is a strong enough coupling between the particle surface and liquid crystal orientation (so-called surface anchoring effects). Then these defects strongly influence the motion of particles. Here we study this problem by using a novel numerical simulation method which incorporates elastic and nematohydrodynamic couplings properly. We find that the surface anchoring properties change both direction and speed of motion of a particle driven in an oriented nematic liquid crystal. This principle may be used for separating particles in terms of their surface properties.

M This article features online multimedia enhancements

(Some figures in this article are in colour only in the electronic version)

Recently there has been a considerable interest in colloidal particles suspended in an anisotropic solvent [1–10]. When particles are immersed in a nematic liquid crystal, the director field of the nematic solvent around them is distorted due to the anchoring on the particle surface. For a case of homeotropic anchoring, for example, three types of defect structures, dipole (hedgehog), Saturn-ring, and surface-ring configuration, are known to be formed in a nematic phase around a particle, depending upon the anchoring property and the particle size [1]. This

elastic coupling between particles and nematic liquid crystal leads to rich static and dynamic behaviour [1, 7–10]. We may expect that a driven particle in an anisotropic nematic liquid exhibits unconventional exotic motion, depending upon surface anchoring properties of the particle. This may be used for surface-sensitive particle separation. A recent proposal of a special type of lyotropic liquid crystal that is water-based but non-surfactant and non-toxic (so-called lyotropic chromonic liquid crystal) opens up novel possibilities to disperse biological molecules and proteins in nematic liquid crystals [11]. Recent studies also suggest a possibility of homogeneous dispersion of colloidal particles accompanying defects in a nematic liquid crystal without aggregation up to a few volume % [5]. Thus, it may be possible to disperse colloidal particles or biological molecules in a liquid crystal homogeneously. In this letter, we demonstrate that by driving them by applying an external field we may perform surface-sensitive particle separation, using the dependence of particle motion on surface anchoring properties.

The understanding of motion of such an externally driven particle in a fluid is the basis for electrophoresis [12] and sedimentation [13], which inevitably involve complex hydrodynamic couplings between particle motion and the degrees of freedom of the host fluid. The dynamics of nematic liquid crystals is linked to their peculiar hydrodynamics (known as nematohydrodynamics) due to coupling between flow and director fields [14, 15]; for example, the reorientation of the director field, which is used in electro-optical devices (e.g. displays), is known to induce internal backflow and to affect the dynamic function of devices. Although the basic hydrodynamics of liquid crystals is reasonably established [16], the dynamics of a mixture of colloids and liquid crystal are still largely unknown. Since the local shear viscosity of liquid crystal depends upon the local nematic order parameter [16], the motion of a particle cannot be described by a simple Stokes law, which has been shown by theories and numerical simulations [1, 17–23]. For example, Ruhwandl and Terentjev [17] studied the drag of a particle with a Saturn-ring defect (e.g. figure 1(b)) and demonstrated that the friction depends upon the angle between the applied force and the director field of the background nematic solvent. During motion parallel to the direction of the directors, the friction is smaller than in the perpendicular case. However, most previous studies dealt with steady particle motion at low Ericksen numbers. The Ericksen number Er is a key parameter characterizing the ratio of the viscous frictional force to the elastic force stored in a nematic liquid crystal. For small Er, we can neglect nonlinear effects and can assume a linear relation between the drag force and the drag velocity, which simplifies the problem. However, intriguing behaviour characteristic to colloids in a nematic solvent may occur at high Ericksen numbers. For example, Stark and Ventzki [21, 22] studied a case of a particle with a hedgehog dipole defect and revealed its non-linear Stokes drag and the coupling between the translational and rotational motion of the particle. In this letter, we report exotic behaviours at higher Er, including cases of highly nonlinear, nonsteady particle motion.

As described above, the hydrodynamics of a nematic liquid crystal with topological defects at high Ericksen numbers is too complex for analytical studies, but may be tackled by numerical simulation. Previous numerical simulation methods have been limited to rather particular situations; for example, the particle positions have to be fixed. To describe the dynamics from a single-particle to a many-particle system in a unified manner, it is highly desirable to develop an efficient numerical simulation method that properly incorporates the dynamical coupling of the relevant field variables, i.e. particle positions $\boldsymbol{r}_n$, orientational order parameter Q_{ij}, and flow field $\boldsymbol{v}$. Molecular dynamics simulation is one possibility for including these three variables, but it is rather slow. Here we propose a new numerical method that incorporates these three variables in a physically natural manner. To simulate colloidal suspensions, the hydrodynamic interaction between particles is one of the most serious obstacles because of its dynamic and

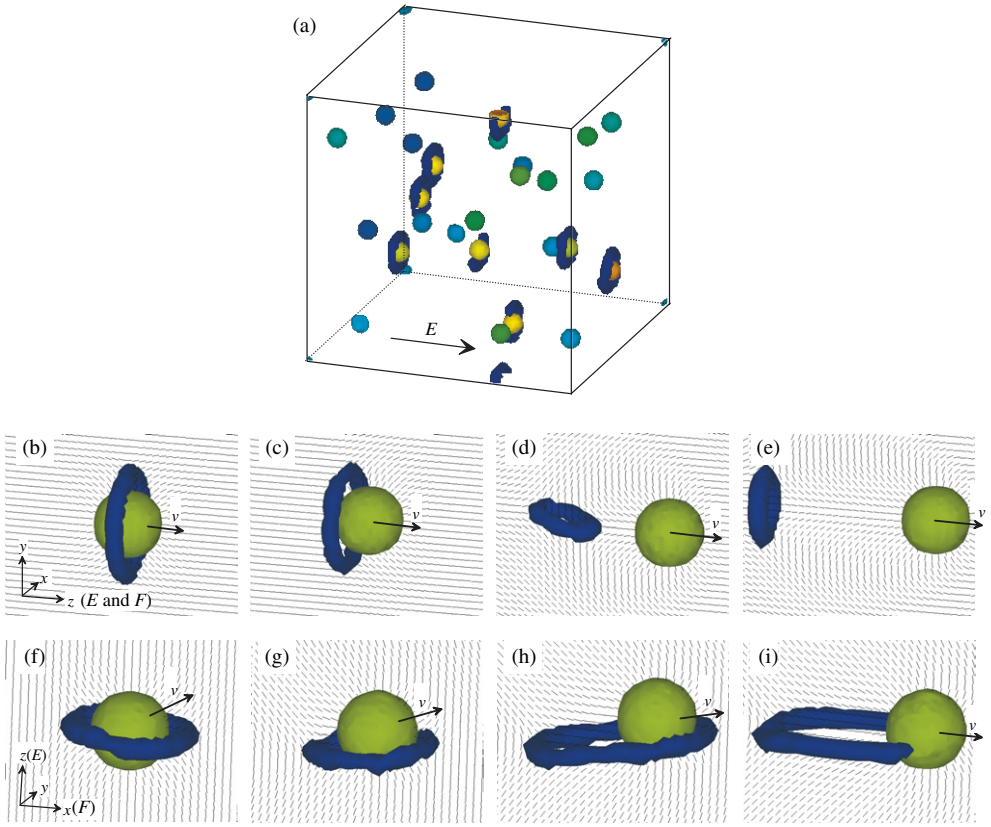

Figure 1. (a) Snapshot of particles ($a = 70$ nm) dispersed in a nematic solvent. The volume fraction is 1.8%. The particle has various anchoring strengths in the range $1.25 < W < 3.75$ ($\times 10^{-4}$ N m^{-1}). The particle colour represents a value of W. Note that a Saturn-ring defect is formed above $W_c \approx 2.5 \times 10^{-4}$ N m^{-1} for $a = 70$ nm. ((b)–(i)) The motion of a particle (green) with a Saturn-ring defect (blue) in the nematic phase, whose director field is drawn by black lines. The external forces are applied on particles in parallel ((b)–(e)) and perpendicular ((f)–(i)) to the magnetic field $\boldsymbol{E}$, which is applied to the nematic solvent. The strength of the applied force is $F_z = 1, 5, 30, 50$ pN for (b)–(e) and $F_x = 5, 20, 30, 40$ pN for (f)–(i), respectively. Note that (b)–(d) and (f)–(g) are steady-state configurations. The thick arrow represents the direction of particle motion. The simulated lattice size is $64 \times 64 \times 64$. See also the supplementary videos available at stacks.iop.org/JPhysCM/18/L193 (movies (b)–(i)).

long-range nature. The difficulties arise from the non-slip boundary condition (discontinuity) on the surface of particles. To get rid of the difficulties, we introduced a smooth interface approximation [24], which renders us able to describe the particle distribution by a continuous field variable $\phi_n(\boldsymbol{r})$. A key feature of our method is to regard a solid colloidal particle as an undeformable fluid one having much higher viscosity than that of the surrounding host liquid. Thus, we called the method the 'fluid particle dynamics (FPD)' method [24]. We assume that viscosity changes smoothly across the particle–solvent interface (the thickness ξ). Thus, we can remove the solid–fluid boundary condition, which is the origin of the difficulties. This description of the particle distribution by a continuous field allows us to straightforwardly incorporate other continuous field variables such as velocity and director fields [25–27]. By using this novel simulation method, we study the motion of a driven particle immersed in a

nematic liquid crystal, including cases of high Ericksen numbers, revealing exotic behaviour. We elucidate the nature of complex dynamic couplings between particle motion and the degrees of freedom of nematic liquid crystal and demonstrate the application to particle separation.

Here we explain the details of our new simulation method based on FPD [24]. The coarse-grained variables relevant for physically describing the dynamics of colloidal systems with anisotropic host fluids are the colloidal particle positions $\boldsymbol{r}_n$, the nematic order parameter Q_{ij} [16] and fluid velocity field $\boldsymbol{v}$. The index n stands for an individual particle. We express fluid particle n using a function $\phi_n(\boldsymbol{r})$ as $\phi_n(\boldsymbol{r}) = [\tanh\{(a - |\boldsymbol{r} - \boldsymbol{r}_n|)/\xi\} + 1]/2$, where a and ξ are the radius and the interface width of the particle, respectively [24]. For the particle dispersion in nematic liquid crystal, we employ the following free energy functional:

$$U\{Q_{ij}, \phi\} = \int \mathrm{d}\boldsymbol{r} \left\{ f(Q_{ij}, \phi) + \frac{K_1}{2} \left(\partial_k Q_{ij}\right)^2 + \frac{K_2}{2} \left(\partial_i Q_{ij}\right)^2 - W\xi\, Q_{ij} \partial_i \phi \partial_j \phi - E_i E_j Q_{ij} \right\}. \tag{1}$$

The first term of equation (1) is the free energy of the bulk nematic phase:

$$f(Q_{ij}, \phi) = -\frac{A}{2}\left(1 - \frac{\phi}{\phi^*}\right) Q_{ij} Q_{ji} - \frac{B}{3} Q_{ij} Q_{jk} Q_{ki} + \frac{C}{4} \left(Q_{ij} Q_{ji}\right)^2, \tag{2}$$

where A, B and C are the positive constants. In the region where $\phi > \phi^*$, a system becomes isotropic. In this study, we employed $\phi^* = 0.5$ such that the inside of each particle should always be in an isotropic state. The second and third terms of equation (1) represent the Frank elastic energy, and K_1 and K_2 are the elastic moduli. Our preliminary simulation indicates that the second elastic term (K_2) does not affect our results presented below significantly, although we keep K_2 in our simulation. Thus, we regard $\Xi = \sqrt{K_1/A}$ as the characteristic length of the nematic phase and use it as a unit of the length. On the other hand, we neglect the bend-splay elastic mode K_{23}. The fourth term is the anchoring energy of the liquid crystal on the particle surface and W represents the anchoring energy per unit area. For $W < 0$ and $W > 0$, the orientational field tends to align parallel (planar) and perpendicular (homeotropic) to the surface of the particle, respectively. The fifth one represents the effect of an applied external field $\boldsymbol{E}$ (described below). In this study, we impose a weak external magnetic or electric field $\boldsymbol{E}$ to realize a homogeneous director field of the background nematic solvent in the simulation box. However, we note that the field strength is kept weak enough to avoid other field effects on the results shown below.

The time development equations for the orientational order Q_{ij} and the flow field $\boldsymbol{v}$ are given by

$$\frac{\mathrm{D}}{\mathrm{D}t} Q_{ij} = Q_{ik}\Omega_{kj} - \Omega_{ik} Q_{kj} + \frac{1}{\mu_1} h_{ij} + \frac{\mu_2}{2\mu_1} A_{ij} + \lambda_{ij}, \tag{3}$$

$$\rho \frac{\mathrm{D}}{\mathrm{D}t} v_i = F_i - \phi \partial_i \mu + Q_{jk} \partial_i h_{jk} + \partial_j \left(h_{ik} Q_{kj} - Q_{ik} h_{kj}\right) - \partial_i p + \partial_j \Sigma_{ij}. \tag{4}$$

Here, $\mu = \frac{\delta}{\delta\phi} U$ and $h_{ij} = -\{\frac{\delta}{\delta Q_{ij}} U - \frac{1}{d}\delta_{ij}\delta_{kl}\frac{\delta}{\delta Q_{kl}} U\}$ are the effective chemical potential for particle concentration ϕ and the molecular force field for nematic order Q_{ij}, respectively [28]. $A_{ij} = \frac{1}{2}\left(\partial_i v_j + \partial_j v_i\right)$ and $\Omega_{ij} = \frac{1}{2}\left(\partial_i v_j - \partial_j v_i\right)$ are symmetric and asymmetric velocity gradient tensors. Σ_{ij} is a mechanical stress tensor for flow field [29]:

$$\Sigma_{ij} = \beta_1(\phi) Q_{ij} Q_{kl} A_{kl} + \left(\beta_4 - \frac{\mu_2^2}{2\mu_1}\right) A_{ij} + \frac{\beta_5 + \beta_6}{2}\left(Q_{ik} A_{kj} + A_{ik} Q_{kj}\right) - \frac{\mu_2}{2\mu_1} h_{ij}, \tag{5}$$

where β_1, β_4, β_5, β_6, μ_1 and μ_2 are constants having a dimensionality of viscosity. Following the concept of FPD [24], the shear viscosity depends upon the particle configuration as $\beta_4 = \bar{\beta}_4 + \sum_n \Delta\beta_4\phi_n(\boldsymbol{r})$. Thus $\bar{\beta}_4$ and $\bar{\beta}_4 + \Delta\beta_4$ correspond to the shear viscosity of the outside and inside of the fluid particle, respectively. $\boldsymbol{F}(\boldsymbol{r})$ is the force field calculated from the force directly acting on particle n, $\boldsymbol{F}_n$, which is independent of $\boldsymbol{E}$: $\boldsymbol{F}(\boldsymbol{r}) = \sum_n \boldsymbol{F}_n\phi_n(\boldsymbol{r})/\int \mathrm{d}\boldsymbol{r}\,\phi_n(\boldsymbol{r})$. Note that direct interparticle interactions such as the Lennard-Jones one can easily be introduced for a many-particle system through $\boldsymbol{F}_n$. λ_{ij} in equation (3) is the thermal noise for Q_{ij}. In the above, we assume that the density of a colloidal particle is the same as that of the host fluid; thus, the density ρ is spatially homogeneous. The pressure p is determined to satisfy the incompressibility condition $\partial_i v_i = 0$. The time evolution of the position of particle n is then described by the average fluid velocity inside the particle as [24]

$$\frac{\mathrm{d}}{\mathrm{d}t}\boldsymbol{r}_n = \int \mathrm{d}\boldsymbol{r}\,\boldsymbol{v}(\boldsymbol{r})\phi_n(\boldsymbol{r}) \Big/ \int \mathrm{d}\boldsymbol{r}\,\phi_n(\boldsymbol{r}). \tag{6}$$

It should be noted that the approximations employed above become exact in the limit of $\Delta\beta_4/\bar{\beta}_4 \to \infty$ and $\xi/a \to 0$ [24].

Here we describe the details of our simulation. The length, time, and force are normalized by the characteristic length $\Xi = \sqrt{K_1/A}$, the characteristic rotational time $\tau_Q = \mu_1\Xi^2/K_1$, and the elastic modulus K_1, respectively. The external magnetic field is also scaled by $\sqrt{K_1Q^2/(\Xi^2\Delta\chi\mu_0)}$. We set B and C as $B/A = 25$ and $C/A = 20$. We define Q as the degree of nematic orientational order below the isotropic–nematic transition as $Q = (B + \sqrt{B^2 + 24AC})/(6C)$. Hereafter, the scaled value of a variable x is denoted as $\tilde{x}$. Throughout this paper, we employ the following parameters. The characteristic length is $\Xi = 2\times10^{-8}$ m, the Frank elasticity is $K_\mathrm{F} = K_1Q^2 = 5\times10^{-13}$ N, the characteristic rotational time is $t_Q = 5.2\times10^{-6}$ s, and the shear viscosity is $\eta = 10^{-2}$ Pa s. The external alignment field $\boldsymbol{E}$ is scaled as $E_0 = \sqrt{K_\mathrm{F}/(\Xi^2\Delta\epsilon)} = 2.6\times10^7$ V m^{-1} ($\Delta\epsilon = 1.8\times10^{-12}$ F m^{-1}) for electric field or $E_0 = \sqrt{K_\mathrm{F}/(\Xi^2\Delta\chi\mu_0)} = 1\times10^8$ A m^{-1} ($\Delta\chi\mu_0 = 1.25\times10^{-13}$ H m^{-1}) for magnetic field. The Reynolds number $\rho K_1/(\eta\mu_1) = 0.02$, the ratio between the two Frank elasticity moduli is $K_2/K_1 = 0.5$, and the ratios among the viscosities of the nematic phase are $\mu_1Q^2/\eta = 0.65$, $-\mu_2/(2\mu_1Q) = 2.0$, $(\beta_5+\beta_6)Q/(2\eta) = 0.06$, and $\beta_1Q^2/\eta = 0.1$. The viscosity ratio between the inner and outer part of a particle is set to be $(\bar{\beta}_4 + \Delta\beta_4)/\bar{\beta}_4 = 50$.

We solve the time development of the particle positions and the orientational field (see equation (3)) using the explicit Euler scheme, whereas that of the flow field (see equation (4)) by the MAC (makers and cell) method with a staggered lattice, in which we set the time increment to be $\Delta\tilde{t} = 0.01$. In this study, we set $\xi = \Xi$ for simplicity and employ ξ as a lattice size.

Next we mention a useful technique employed in our simulation. The orientational order parameter $Q_{ij} = \frac{3}{2}Q[n_in_j - (1/3)\delta_{ij}]$, which is a traceless and symmetric tensor, has five ingredients in 3D. However, only three of them are independent of each other. In computation, it is not easy to choose these three variables from the five since x, y, and z axes have to be treated equally. For example, we can take Q_{xx}, Q_{yy}, and Q_{xy} as the three independent ingredients; in this case, however, here the z axis is treated specially. Furthermore, Q_{xx}, Q_{yy}, and Q_{zz} cannot be the three independent ingredients. To overcome this problem, we solve the dynamics of the tensor field using the vector, which is defined as $q_i = Qn_i$. Using a vector q_i, the tensorial order Q_{ij} and its time development is easily calculated, using the relations $Q = \sqrt{q_iq_i}$ and $n_i = q_i/Q$. In this scheme, the time development of q_i is described as $\dot{q}_i = \dot{Q}_{jk}\{n_in_jn_k + (d-1)\delta_{ik}n_j\}/d$ (d: the spatial dimensionality).

In our simulation, a Saturn-ring defect is formed around a particle under an alignment field $\boldsymbol{E}$ along the z axis (figure 1(b)). This field $\boldsymbol{E}$ is used to align the nematic director and can be an electric, magnetic, or surface field. In figure 1, we applied an external field

corresponding to an electric field $E_z = 1.3$ V mm^{-1} or a magnetic field $E_z = 5.0$ A mm^{-1}. Figure 1(a) shows a snapshot of particles of radius $a = 70$ nm dispersed in a nematic solvent. The volume fraction is 1.8%. The particles are rather homogeneously suspended for this volume fraction, which is suitable for particle separation. The particles have various anchoring strengths in the range $1.25 < W < 3.75$ ($\times 10^{-4}$ N m^{-1}). When the mass, charge, and size of the particle are the same as those of other particles, it is difficult to separate them with conventional methods. However, if the particles have different surface properties as in figure 1(a), they may be separated in terms of the surface properties, using a nematic solvent as a host liquid. To check this, we apply a constant force directly on the single particle ($a = 120$ nm; $W = 2.5 \times 10^{-4}$ N m^{-1}) either parallel (along the z axis) or perpendicular (along the x axis) to the director field of the background nematic solvent; i.e., $(0, 0, F_z)$ and $(F_x, 0, 0)$, respectively. Figures 1(b)–(i) show simulated snapshots of a particle (green) accompanying a Saturn-ring defect (blue) for both $\boldsymbol{E} \parallel \boldsymbol{F}$ ((b)–(e)) and $\boldsymbol{E} \perp \boldsymbol{F}$ ((f)–(i)).

First we consider a case of $\boldsymbol{E} \parallel \boldsymbol{F}$. In this case, a particle always moves along the applied force $\boldsymbol{F}$. For a weak force, the relative position of the defect to the particle almost remains the most stable position at rest (figure 1(b)). With an increase in $F = |\boldsymbol{F}|$, the defect position tends to be shifted backward from the original configuration, as shown in figure 1(c). As the separation between the particle and defect approaches the particle size with an increase in F, the ring defect gradually shrinks. As the separation becomes even larger, the defect tends to be inclined and elongated along $\boldsymbol{F}$ (figure 1(d)). The plane of a ring defect is selected randomly under the constraint to be tangential to a cone axisymmetric about the z axis. This configuration may be selected to reduce the dissipation due to the friction between the defect and the nematic solvent. However, the defect can still follow the particle with a delay and the motion of a particle with defect eventually reaches a steady state. For a force beyond a certain strength, on the other hand, the defect cannot catch up with the particle anymore; in other words, it escapes from the particle, as shown in figure 1(e). In this case, a steady state is never observed; namely, the separation between the particle and the defect and the resulting stored elastic energy excess to that at rest ($F = 0$), ΔU, both increase with time. However, when ΔU exceeds the energy gain due to the formation of a Saturn-ring defect, the surface anchoring is removed, or the defect disappears; then ΔU should stop increasing. We note that the escape of the defect does not break the axial symmetry of the particle motion with respect to the surrounding director field and thus a particle moves along the force applied.

For $\boldsymbol{E} \perp \boldsymbol{F}$, we observe even more exotic behaviour. For a weak force, the defect almost remains in the most stable configuration at rest (figure 1(f)). Interestingly, however, the particle does not move along the applied force $\boldsymbol{F}$ and is lifted up or down ($v_x, v_z \neq 0$; $v_y = 0$). This is because there is a defect toward the direction of particle motion; since the decrease in the distance between the defect and the particle costs elastic energy, the defect acts as an obstacle for the particle motion. Since $\boldsymbol{F}$ is set to be completely perpendicular to $\boldsymbol{E}$, the two directions of motion in parallel to the z axis are equivalent and thus one of them is randomly selected by the thermal noise in each simulation. We can intentionally break this symmetry by pulling the particle in a slightly different direction. With an increase in the force, the defect position is slightly shifted from the particle centre (figure 1(g)). Unlike the case of $\boldsymbol{E} \parallel \boldsymbol{F}$, however, the defect cannot easily escape from the particle even for a strong applied force. When the force exceeds a certain threshold, the rear part of the defect becomes retarded from the particle (figure 1(h)). The defect becomes more and more elongated with time, and does not reach a steady state. If we increase the force further, the front part of the defect enters the particle (figure 1(i)). This penetration of the defect into the particle indicates the loss of anchoring at the front surface. It is worth noting that for both cases the deformed director field recovers the original configuration at rest if the applied force is turned off.

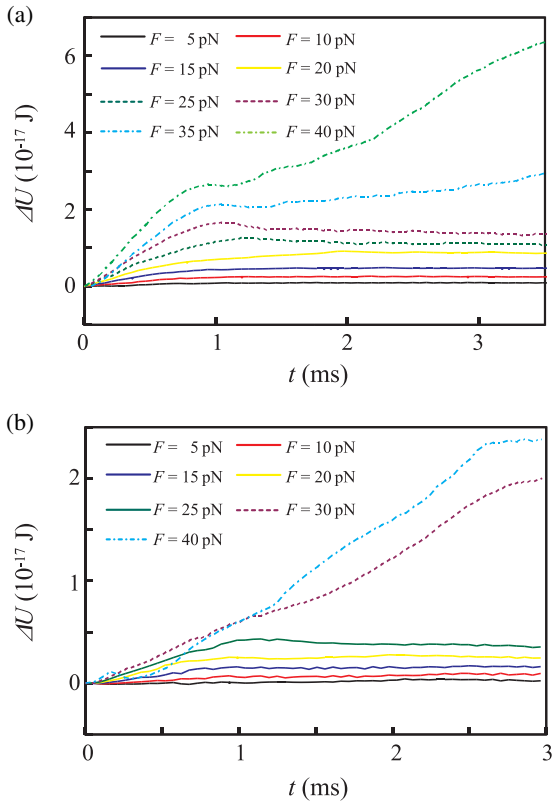

Figure 2. Time evolution of the stored elastic energy for various strengths of the applied force. (a) $\boldsymbol{E} \parallel \boldsymbol{F}$ and (b) $\boldsymbol{E} \perp \boldsymbol{F}$. The solid, dashed, and chain-dashed lines correspond to figures 1(b) and (c), (d) and (e) for $\boldsymbol{E} \parallel \boldsymbol{F}$ and (f) and (g), (h) and (i) for $\boldsymbol{E} \perp \boldsymbol{F}$, respectively.

It has been known [17] that the motion of a particle in a nematic solvent is not necessarily along the applied force, and the Stokes law for this situation is described as $\boldsymbol{F} = \bar{\gamma}\boldsymbol{v}$ with $\bar{\gamma} = \gamma_\perp \bar{I} + (\gamma_\parallel - \gamma_\perp)\boldsymbol{z} \otimes \boldsymbol{z}$, for small Er. Here $\gamma_\parallel$ and $\gamma_\perp$ are the effective friction coefficients for the parallel and perpendicular motion of a particle in a uniform nematic fluid, respectively, $\boldsymbol{z}$ is the unit vector along the background nematic solvent (z axis), and $\otimes$ is the dyad operator producing a tensor from two vectors. This relation tells us that a particle moves along the z direction only if the force is perpendicular or parallel to the direction of the field (z direction). In our simulation of $\boldsymbol{E} \perp \boldsymbol{F}$, however, the Stokes drag cannot be described by the above simple relation, which predicts the motion along the force for this geometry. The symmetry of the motion is spontaneously broken due to the presence of an obstacle in front of it and the system enters a new type of a nonsteady state. This indicates the breakdown of the linear approximation that the director field does not contribute to the dynamics, which is satisfied at low Ericksen numbers.

Figures 2(a) and (b) show the time evolution of the stored elastic energy (see equation (1)) for $\boldsymbol{E} \parallel \boldsymbol{F}$ and $\boldsymbol{E} \perp \boldsymbol{F}$, respectively. When the applied force is weaker than a critical value, ΔU increases with time in the early stage, but reaches the steady state value for $t > 1$ ms. ΔU in the steady state is roughly proportional to the force strength F for both figures 2(a) and (b). For a force beyond a critical value, on the other hand, the elastic energy grows with time indefinitely, which indicates the escape of the defect from the particle (figures 1(e), (h), and (i)).

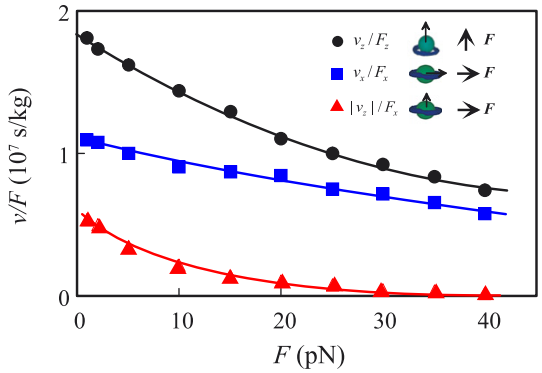

Figure 3. Dependence of the particle mobility v/F on the strength of the force F for $\boldsymbol{E} \parallel \boldsymbol{F}$ and $\boldsymbol{E} \perp \boldsymbol{F}$. For $\boldsymbol{E} \perp \boldsymbol{F}$, the particle does not move along the force; thus, we plot the two mobilities, which are in parallel and perpendicular to the force (see the inset figure). Note that the absolute value $|v_z|/F_x$ is plotted for the lift-up mobility since the two directions of the motion along the z axis are equivalent. Here we note that the absolute value of the frictional force from the solvent significantly depends upon the simulation box size [24].

The critical force, beyond which the defect escapes from the particle, is $F_z \approx 30$ pN for $\boldsymbol{E} \parallel \boldsymbol{F}$. For $\boldsymbol{E} \perp \boldsymbol{F}$, on the other hand, there exist two characteristic forces, $F_x \approx 25$ and 35 pN, which correspond to the escape of the rear part of the defect (figure 1(f)) and the penetration of the front part into the particle (figure 1(g)), respectively. For $\boldsymbol{E} \parallel \boldsymbol{F}$, we can see the overshoot behaviour in ΔU for $F_z > 20$ pN before ΔU reaches the steady state value. The overshoot behaviour reflects the change in the orientation and shape of the ring defect (figure 1(d)), which occurs when the separation between the particle and the defect becomes of the order of the particle size. Similar behaviour is also seen for $F_z > 35$ pN, where the defect cannot follow the particle any more. The overshoot behaviour suggests the existence of an energy barrier for transformation between a Saturn-ring defect configuration and the others [1].

Figure 3 shows the dependence of the particle mobility on the strength of a driving force. As described before, the particle moves along the applied force (mobility v_z/F_z) for $\boldsymbol{E} \parallel \boldsymbol{F}$. For $\boldsymbol{E} \perp \boldsymbol{F}$, on the other hand, it does not move along the force. Thus, the particle has a component of the velocity along the orientation of the background nematic solvent ($|v_z|/F_x$) as well as that along $\boldsymbol{F}$ (v_x/F_x). We note that the mobility of the particle moving in an isotropic solvent having the same viscosity η is estimated to be $v/F \approx 2.3 \times 10^7$ s kg^{-1} here.

For $\boldsymbol{E} \parallel \boldsymbol{F}$, the mobility decreases with an increase in force. This is because part of the applied force is used to shift the position of the defect relative to the particle, paying the resulting elastic energy cost. For $\boldsymbol{E} \perp \boldsymbol{F}$, the mobility along the applied force also decreases with an increase in the force, although the degree of the nonlinearity is weaker than for $\boldsymbol{E} \parallel \boldsymbol{F}$. On the other hand, the mobility normal to the force becomes significantly smaller for large F. This means that the ratio, $|v_z|/v_x$, decreases with an increase in $\boldsymbol{F}$; namely, the particle motion is more aligned along the direction of the applied force for stronger $\boldsymbol{F}$. The mobility is always larger for $\boldsymbol{E} \parallel \boldsymbol{F}$ than for $\boldsymbol{E} \perp \boldsymbol{F}$, but its difference becomes smaller with an increase in the force. Finally we note that there is no discontinuous change in the mobility around the critical values of $\boldsymbol{F}$.

Here we show an example of surface-sensitive particle separation. Figures 4(a) and (b) represents the motion of three particles with different anchoring strengths W immersed in a nematic liquid crystal aligned such that $\boldsymbol{E} \perp \boldsymbol{F}$. A particle with strong surface anchoring changes the direction of motion, whereas a particle with weak or no anchoring moves along

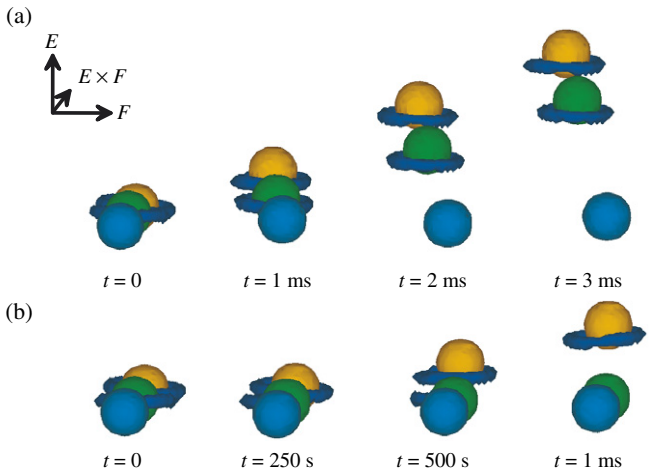

Figure 4. Demonstration of surface-sensitive particle separation. Particles with different anchoring strengths are dragged by an external force $\boldsymbol{F} = 6$ pN (a) and $\boldsymbol{F} = 20$ pN (b) in a nematic liquid crystal aligned such that $\boldsymbol{E} \perp \boldsymbol{F}$. The anchoring strengths of the blue, green, and red particles (bottom to top) are $W = 1.5$, 2.0, and 2.5×10^{-4} N m^{-1}, respectively.

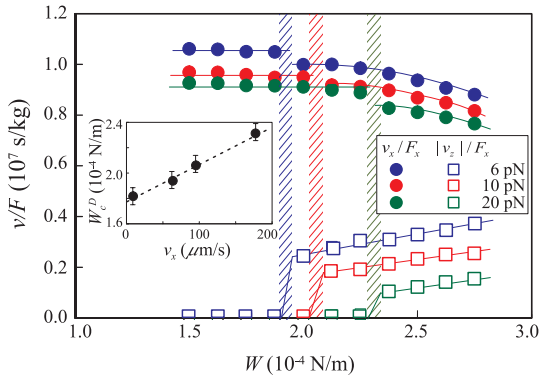

Figure 5. Dependence of the particle mobility both parallel and perpendicular to the field on the anchoring strength W and the driving force F_x. The inset shows the relationship between W_c^D and v_x.

the driving force. The threshold value of W, which separates $v_z = 0$ and $v_z \neq 0$, depends upon the driving force F_x (compare figures 4(a) and (b)). This means that the direction and speed of particle motion are crucially dependent upon both the surface anchoring properties and the force F_x. Figure 5 shows the dependence of the particle mobility both parallel and perpendicular to the field on the anchoring strength W. The threshold anchoring strength in the dynamic situation W_c^D increases with an increase in the particle velocity v_x (see below and the inset of figure 5). We can also see a sharp change of the direction of motion at W_c^D as well as the monotonic decrease of the mobility with an increase in W above W_c^D. This correlation among the particle mobility, the direction of motion, the anchoring strength, and the driving force may be applied to separation of particles in terms of the surface properties.

Finally we discuss physical mechanisms responsible for this exotic behaviour. First we consider the defect escape from a particle (figures 1(b)–(i)). We note that the key process of

defect motion is the director rotation. Thus, the relevant viscosity for the Ericksen number is the rotational viscosity μ_1, and not the shear viscosity η as often assumed. Then the frictional force is calculated as $\mu_1 v/\Xi$, where Ξ is the characteristic director correlation length, or the characteristic size of the defect core. The characteristic elastic force is, on the other hand, K_1/Ξ^2, where K_1 is the Frank elastic constant. Thus, the relevant Ericksen number of this problem is $Er = \mu_1 v \Xi/K_1$: for $Er \gtrsim 1$, the director rotation cannot follow the deformation rate induced by the particle motion. In our simulation, the defect escape occurs at $Er \approx 1.1$ and 0.8 for $\boldsymbol{E} \parallel \boldsymbol{F}$ and $\boldsymbol{E} \perp \boldsymbol{F}$, respectively. This is consistent with the above prediction. The threshold for $\boldsymbol{E} \perp \boldsymbol{F}$ is slightly lower than that for $\boldsymbol{E} \parallel \boldsymbol{F}$. This may be because the shear rate is higher at the front and back of the particle than at its sides. If our scenario is correct, the escape of the defect is easier for larger μ_1. We confirm this prediction for $\boldsymbol{E} \perp \boldsymbol{F}$, which supports the above-proposed mechanism based on the dynamic crossover. We found that the coupling viscosity μ_2 also affects the threshold, especially for $\boldsymbol{E} \parallel \boldsymbol{F}$, the details of which will be discussed elsewhere.

Next we consider the phenomenon of defect penetration into a particle for $\boldsymbol{E} \perp \boldsymbol{F}$ (figures 1(d)–(g)). Since the surface anchoring on the front surface has to be removed upon the defect penetration, the anchoring strength should play an important role in this phenomenon. The force pushing the defect toward the particle is to be the Stokes frictional force $F_v = \eta v \Xi^2/a$. The energy cost for the front part of the defect to penetrate into the particle is, on the other hand, estimated as $(W - W_c) Q l^2$. Here l is the separation between the two contacting points of the defect along the equator of the particle and thus l^2 is related to the area where the homeotropic anchoring is destroyed. W_c is the threshold of the anchoring strength, below which a Saturn-ring defect becomes unstable. From a simple scaling argument, we obtain $W_c = C K_1/a$, where C is a non-dimensional constant ($C \approx 41$ in our simulation). Thus, the force recovering the penetrating defect to the Saturn ring is roughly estimated as $F_a = \beta(W - W_c) Q l$, where β is a non-dimensional constant ($\beta \approx 0.3$ in our simulation). By equating F_v and F_a, we obtain the critical separation as $l_c = \eta v \Xi^2/\beta\{(W - W_c) Q a\}$. For $l_c > \Xi$, a front part of the Saturn-ring defect penetrates into the moving particle. For a stronger applied force, l_c approaches the particle size a. In this situation, the entire defect cannot follow the particle and the defect itself becomes unstable and eventually disappears (see the middle green particle in figure 4(b)). This threshold for the defect disappearance, $W_c^D(v_x)$, for a driven particle is estimated as $W_c^D - W_c = \eta v_x \Xi^2/(\beta Q a^2)$. This is consistent with the relationship between W_c^D and v_x, which is shown in the inset of figure 4(c). Since the defect escape and penetration are independent of each other, for small $(W - W_c)$ the penetration of the front part of the defect into the particle may take place earlier than the escape of the rear part from the particle with an increase in the force.

To summarize, we demonstrate a new possibility of surface-sensitive particle selection by using nematic liquid crystal as a solvent. We have developed a novel coarse-grained simulation method that can simulate a moving colloidal particle in a liquid crystal including (nemato)hydrodynamics, surface anchoring, and elastic effects (note that our colloid is not fixed at a certain spatial point) and is also capable of multi-particle simulations. Using this simulation method, we have demonstrated that the surface anchoring properties change both direction and speed of motion of a particle driven in an oriented nematic liquid crystal and proposed a novel principle of particle separation.

The authors are grateful to C P Royall for a critical reading of our manuscript. This work was partially supported by a grant-in-aid from the Ministry of Education, Culture, Sports, Science and Technology, Japan.

References

[1] Stark H 2001 *Phys. Rep.* **351** 387
[2] Poulin P, Stark H, Lubensky T C and Weitz D A 1997 *Science* **275** 1770
[3] Poulin P, Cabuil V and Weitz D A 1997 *Phys. Rev. Lett.* **79** 4862
[4] Meeker S P, Poon W C K, Crain J and Terentjev E M 2000 *Phys. Rev.* E **61** R6083
[5] Anderson V J, Terentjev E M, Meeker S P, Crain J and Poon W C K 2001 *Eur. Phys. J.* E **4** 11
[6] Yamamoto J and Tanaka H 2001 *Nature* **409** 321
[7] Terentjev E M 1995 *Phys. Rev.* E **51** 1330
[8] Ruhwandl R W and Terentjev E M 1997 *Phys. Rev.* E **56** 5561
[9] Stark H 1999 *Eur. Phys. J.* B **10** 311
[10] Fukuda J and Yokoyama H 2001 *Eur. Phys. J.* E **4** 389
[11] Shiyanovskii S V, Schneider T, Smalyukh I I, Ishikawa T, Niehaus G D, Doane K J, Woolverton C J and Lavrentovich O D 2005 *Phys. Rev.* E **71** 020702(R)
[12] Viovy J-L 2000 *Rev. Mod. Phys.* **72** 813
[13] Lebowitz J, Lewis M S and Schuck P 2002 *Protein Sci.* **11** 2067
[14] Tóth G, Denniston C and Yeomans J M 2003 *Phys. Rev.* E **67** 051705
[15] Svenšek D and Žumer S 2002 *Phys. Rev.* E **66** 021712
[16] de Gennes P G and Prost J 1993 *The Physics of Liquid Crystals* (Oxford: Clarendon)
[17] Ruhwandl R W and Terentjev E M 1996 *Phys. Rev.* E **54** 5204
[18] Chono S and Tsuji T 1998 *Mol. Cryst. Liq. Cryst.* **309** 217
[19] Billeter J L and Pelcovits R A 2000 *Phys. Rev.* E **62** 711
[20] Stark H and Ventzki D 2001 *Phys. Rev.* E **64** 031711
[21] Stark H and Ventzki D 2002 *Europhys. Lett.* **57** 60
[22] Stark H, Ventzki D and Reichert M 2003 *J. Phys.: Condens. Matter* **15** S191
[23] Fukuda J, Stark H, Yoneya M and Yokoyama H 2004 *J. Phys.: Condens. Matter* **16** S1957
[24] Tanaka H and Araki T 2000 *Phys. Rev. Lett.* **85** 1338
Tanaka H and Araki T 2006 *Chem. Eng. Sci.* **61** 2108
[25] Yamamoto R 2001 *Phys. Rev. Lett.* **87** 075502
[26] Yamamoto R, Nakayama Y and Kim K 2004 *J. Phys.: Condens. Matter* **16** S1945
[27] Kodama H, Takeshita K, Araki T and Tanaka H 2004 *J. Phys.: Condens. Matter* **16** L115
[28] Araki T and Tanaka H 2004 *Phys. Rev. Lett.* **93** 015702
[29] Qian T and Sheng P 1998 *Phys. Rev.* E **58** 7475